Validation of a Partitioned Fluid-Structure Interaction Simulation for Turbo Machine Rotors

Jorrid Lund[a,*], Daniel Ferreira González[b], Jan Clemens Neitzel-Petersen[b], Lars Radtke[a], Moustafa Abdel-Maksoud[b], Alexander Düster[a]

[a] *Numerical Structural Analysis with Application in Ship Technology (M-10), Hamburg University of Technology (TUHH), Am Schwarzenberg Campus 4 C, 21073 Hamburg, Germany*
[b] *Institute for Fluid Dynamics and Ship Theory (M-8), Hamburg University of Technology (TUHH), Am Schwarzenberg Campus 4 C, 21073 Hamburg, Germany*

Abstract

In the scope of this work, a partitioned solution approach for the fluid-structure interaction (FSI) simulations of turbo machine rotors is presented. The in-house developed boundary element method (BEM) solver *pan*MARE is used for the fluid simulation, while the structural side is treated with the commercial finite element method (FEM) solver ANSYS. The generic in-house multiphysics coupling library *comana* is used for the management of the implicit coupling procedure. As the first example, the KRISO container ship propeller is considered. The corresponding FSI simulation is validated for open water test conditions assuming a rigid propeller based on experimental values for the thrust and torque coefficients. Furthermore, results for a flexible propeller simulated with a partitioned coupled FSI simulation in open water are presented. In the second example, the validation of the fully coupled FSI simulation is conducted for a multilayered flexible submersible mixer based on thrust and torque coefficients. The results show a good agreement between the simulations and the experimental data for the rigid body propeller and the flexible rotor of a submersible mixer.

Keywords: propeller, submersible mixer, open turbo machine, flexible blade, fluid-structure interaction, finite element method, boundary element method, validation

1. Introduction

Marine propellers have been the leading type of propulsion device for commercial shipping for decades. For the shipbuilding industry, it is thus an important challenge to continuously improve and optimise marine propellers. New materials like carbon fibre reinforced polymers (CFRPs) and glass fibre reinforced polymers (GFRP) have led to new developments and designs in the development of marine propellers. CFRP propellers have already been used for large commercial vessels – with promising results [1]. Previous works have demonstrated that flexible marine propellers, apart from reducing the weight, allow for a reduction of cavitation which leads to a decrease in noise emission [2] [3]. Taking advantage of the anisotropy of composite propellers, it is also possible to increase the efficiency [4].

The accurate simulation of marine structures such as propellers is a major challenge for development engineers. It is becoming increasingly important to consider fluid-structure interaction in the scope of hydrodynamic behaviour when using new and more flexible materials like CFRP and GFRP [5]. Not only for propellers but also for many other marine applications (like floating structures) it is important to consider fluid-structure interaction (FSI) so as to obtain reliable simulation results. Apart from the benefits

*Corresponding author. Am Schwarzenberg Campus 4 C, 21073 Hamburg, Germany
Email address: Jorrid.Lund@tuhh.de (Jorrid Lund)

in capturing the modified hydrodynamic behaviour of the flexible structure, FSI simulations also offer the advantage of evaluating the stress inside the structure during the full loading cycle.

For the simulation of FSI problems, it is possible to use monolithic and partitioned coupling strategies. Monolithic coupling schemes are usually faster and more stable, but they require the development of a new dedicated solver that can deal with the fluid and structural problems simultaneously [6]. On the other hand, partitioned coupling schemes offer the possibility to use existing highly specialized and advanced solvers for fluid and structural problems. The disadvantage of partitioned coupling schemes lies in the increased computational effort due to the repetition of time steps and possible instabilities due to the coupling. These disadvantages of the partitioned solution approach can be reduced by using extrapolation and convergence acceleration techniques [7] [8].

For complex simulations, it is of major importance to verify and validate the results in order to prove the reliability of the simulation and to identify the limitations of the approach. Therefore, the aim of this work is to present an approach for the simulation of the fluid-structure interaction of a flexible propeller and to verify and validate the results based on experimental data. The simulation approach presented here will be used in future works to optimise the propeller in terms of noise emissions, thrust and efficiency by modifying the shape and the material.

The in-house developed boundary element method (BEM) solver *pan*MARE [9] is used for the fluid simulation, while the structural side is treated with the commercial finite element method (FEM) solver ANSYS [10]. The generic in-house multiphysics coupling library *comana* [11] is used for the management of the implicit coupling procedure. To capture the fluid-structure interaction of a marine propeller accurately, a two-way coupling approach is applied [11].

To validate the hydrodynamic simulation, studies were carried out on the stiff KRISO container ship (KCS) propeller for which plenty of experimental data is available. Since experimental data on flexible propellers is rare, the validation of the fully coupled FSI approach was conducted on a flexible rotor of a submersible mixer.

The paper is structured as follows. First, the theory and setup of the coupling scheme for the fluid and structural solver are explained. Then the two examples – the KCS propeller and the submersible mixer – are introduced and the results are discussed. At the end, a conclusion and an outlook are given.

2. Partitioned solution approach for FSI-problems

The partitioned solution requires an exchange of data between the fluid and the structural solver. To manage the exchange of data and to control the whole solution process involving implicit coupling, the coupling manager *comana* [11] was developed.

The coupling is carried out on the common interface between the fluid and the structure by transferring displacements $\mathbf{d}$ from the structural to the fluid solver and by transferring tractions $\mathbf{t}$ from the fluid to the structural solver. To fully capture the interaction between the fluid and the structure, multiple exchanges of tractions and displacements between the fluid and structure solvers are necessary at each time step. In other words, the resulting solution must satisfy the boundary conditions in each solver at the same time step. Every time step t begins in the first implicit iteration with a prediction of displacements $\tilde{\mathbf{d}}_1^t$ based on the extrapolation $\mathcal{E}$ of the converged displacements from the previous time steps $(\mathbf{d}^{t-1}, \mathbf{d}^{t-2}, ...)$. With a quadratic extrapolation and a constant time step size the displacements can be, for example, estimated as

$$\tilde{\mathbf{d}}_1^t = \mathcal{E}(\mathbf{d}^{t-1}, \mathbf{d}^{t-2}, \mathbf{d}^{t-3}) = 3\mathbf{d}^{t-1} - 3\mathbf{d}^{t-2} + \mathbf{d}^{t-3}. \tag{1}$$

This relationship can easily be computed by a polynomial extrapolation of previous solutions $\mathbf{d}^{t-1}$, $\mathbf{d}^{t-2}$, $\mathbf{d}^{t-3}$. If there is not enough data available, the extrapolation is reduced in polynomial order or the estimate is set to $\tilde{\mathbf{d}}_1^1 = \mathbf{0}$ in the first time step.

In the implicit iteration loop, the estimated displacements are then transferred to the fluid solver $\mathcal{F}$ in the first iteration $i = 1$ in order to solve for the fluid field and to compute tractions $\mathbf{t}_i^t$ on the interface between the fluid and the structure:

$$\mathbf{t}_i^t = \mathcal{F}(\tilde{\mathbf{d}}_i^t). \tag{2}$$

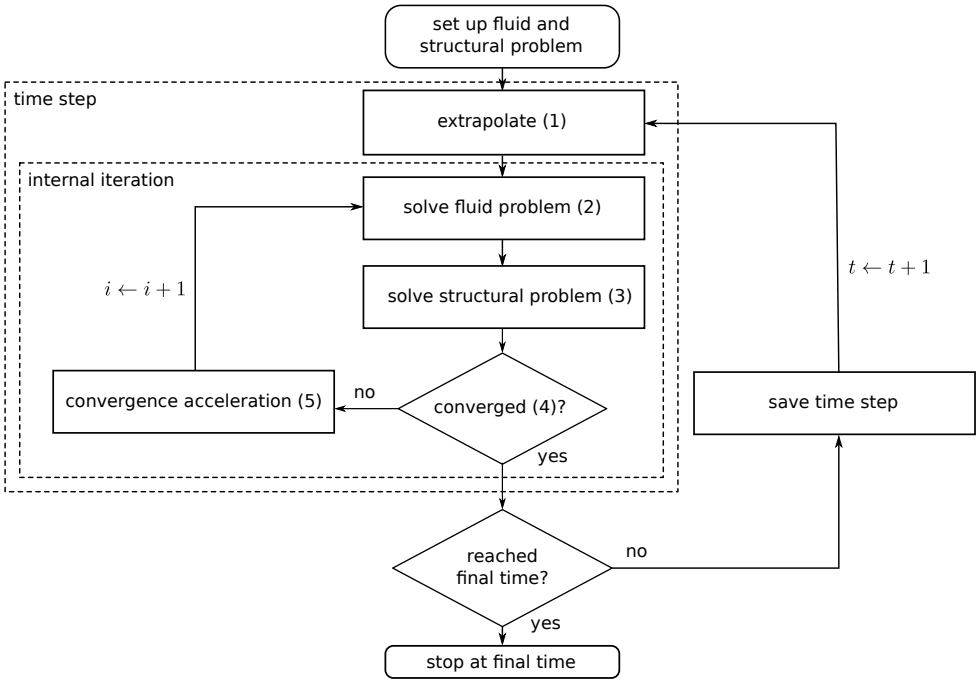

Figure 1: Partitioned coupling solution approach for FSI problems

The tractions computed by the fluid solver in Eq. (2) are then forwarded to the structural solver $\mathcal{S}$. Since the spatial discretization on the interface of the structural and the fluid solver usually do not match, it is necessary to perform an interpolation between the two meshes. The traction values computed by the fluid solver on the interface are interpolated to the integration points of the structural solver.

The structural solver computes new displacements

$$\mathbf{d}_i^t = \mathcal{S}(\mathbf{t}_i^t), \tag{3}$$

which as before must be interpolated to the vertices of the fluid mesh. To check for convergence, a residual $\mathbf{r}_i$ can now be computed in every iteration as

$$\mathbf{r}_i = \mathbf{d}_i^t - \tilde{\mathbf{d}}_i^t. \tag{4}$$

If the norm of the residual falls below a predefined relative or absolute tolerance $\|\mathbf{r}_i\| < TOL$, the solution is considered to be converged and the procedure can continue with the next time step $t = t + 1$.

If the solution has not converged, a convergence acceleration scheme $\mathcal{A}$ can be applied to improve the displacement estimate

$$\tilde{\mathbf{d}}_{i+1}^t = \mathcal{A}(\mathbf{d}_i^t, \mathbf{d}_{i-1}^t, \mathbf{d}_{i-2}^t, ...) \tag{5}$$

for the next iteration $i + 1$ based on the results from the current and previous iterations $(\mathbf{d}_i^t, \mathbf{d}_{i-1}^t, \mathbf{d}_{i-2}^t, ...)$.

The convergence acceleration scheme $\mathcal{A}$ improves the stability and convergence in the implicit coupling solution procedure. It can vary from simple static or dynamic relaxation to more advanced methods such as the Aitken method or quasi-Newton methods. Previous studies indicate that the quasi-Newton least-squares method yields good results for a partitioned coupling of FSI problems [12] [13]. Therefore the quasi-Newton least-squares method is used as the convergence acceleration scheme in this work.

After the convergence acceleration, the next iteration is started and the implicit coupling iterations are continued until convergence is obtained. The whole solution procedure is depicted in Fig. 1.

3. Fluid simulation

For the fluid simulation, the BEM implemented in *pan*MARE [9] is used. *pan*MARE is an in-house code developed by the Institute for Fluid Dynamics and Ship Theory, and it contains a first-order panel method [14] to simulate fluid dynamic problems.

To solve the fluid problem in *pan*MARE, a stationary Cartesian coordinate system (x, y, z), with z pointing upwards against the direction of gravitation g, is defined within the relevant fluid domain Ω_F. Assuming the fluid to be incompressible, irrotational and inviscid, the density ρ is constant and a velocity potential Φ exists which fulfils the Laplace equation

$$\Delta\Phi = \nabla^2\Phi = 0\,. \tag{6}$$

Here, $\nabla = (\partial/\partial x, \partial/\partial y, \partial/\partial z)^T$ is the Nabla operator and Δ denotes the Laplace operator.

Bernoulli's equation provides the hydrodynamic fluid pressure p as follows:

$$p + \rho\left(\frac{\partial\Phi}{\partial t} + \frac{1}{2}\,\nabla\Phi^2 + gz\right) = \text{const.} \tag{7}$$

Taking advantage of the linearity of Laplace's Eq. (6) the velocity potential Φ can be superposed by various solutions. Hence, the velocity potential can be subdivided into two parts

$$\Phi = \phi_\infty + \phi_{\text{ind}}\,, \tag{8}$$

where ϕ_∞ denotes a potential background flow and ϕ_{ind} describes the potential which is induced due to the presence of a body in the fluid. Furthermore, applying Green's second identity, the computation of the unknown induced potential ϕ_{ind} can be regarded as a boundary value problem. Then, the induced potential at a certain position $\mathbf{x}$ can be derived as the solution of the integral over the boundary S:

$$0 = \phi_{\text{ind}}(\mathbf{x}) - \frac{1}{4\pi}\int_S \left(\phi_{\text{ind}}(\mathbf{x}_r)\; G_n(\mathbf{x}, \mathbf{x}_r) - \frac{\partial}{\partial n}\phi_{\text{ind}}(\mathbf{x}_r)\; G(\mathbf{x}, \mathbf{x}_r)\right) \mathrm{d}S\,, \tag{9}$$

with $\mathbf{x}_r$ being the collocation point of the source, $G(\mathbf{x}, \mathbf{x}_r) \equiv 1/(|\mathbf{x}-\mathbf{x}_r|)$ being the source Green function, and G_n its derivative. Different types of boundary conditions can be applied at the boundaries of the fluid domain under consideration. Here, the following boundary conditions are applied:

1. The Dirichlet condition ensures that the potential is constant outside of the simulation domain, thus:

$$\phi_{\text{ind}} = \text{const.} \qquad \text{for} \qquad \mathbf{x} \notin \Omega_F \tag{10}$$

2. The Neumann boundary condition ensures that there is no flow through the body surface. This condition has to be fulfilled at the interface Γ_{FSI}:

$$(\mathbf{v}_0 + \nabla\phi_{\text{ind}} - \mathbf{u}) \cdot \mathbf{n} = 0 \qquad \text{for} \qquad \mathbf{x} \in \Gamma_{FSI}\,, \tag{11}$$

   where $\mathbf{v}_0$ describes an external flow, $\mathbf{u}$ is the motion velocity and $\mathbf{n}$ the normal vector at the interface Γ_{FSI}.

3. The far-field condition ensures that the influence of the induced velocities vanishes with growing distance

$$\lim_{\mathbf{x}\to\infty} \nabla\phi_{\text{ind}} = \mathbf{0}\,. \tag{12}$$

4. The Kutta condition is applied to model the vorticity of the wake at the trailing edge of lifting bodies S_{w}:

$$\Delta p = 0 \qquad \text{for} \qquad \mathbf{x} \in \mathcal{S}_{\text{w}}, \tag{13}$$

   where Δp is the pressure jump between the pressure and the suction side at the trailing edge of the rotor blades.

The numerical method to solve the fluid problem in the present paper is a low-order boundary element method. Here, the surfaces are discretized using panels. The source strength σ and the doublet strength μ are constantly distributed over each panel surface. The strength of source and doublet are defined as follows:

$$\sigma = \frac{\partial \phi_{\mathrm{ind}}}{\partial n}\,, \tag{14}$$

$$\mu = -\phi_{\mathrm{ind}}\,. \tag{15}$$

They refer to the collocation point. A detailed description of the underlying approach is given by [14].

Assuming lifting bodies, the wake has to be considered by wake panels. These panels do not have a source but only a doublet μ_{w}. Substituting the source and doublet strength from Eqs. (14) – (15) for the velocity potential in Eq. (9) yields a formulation for the induced potential at position $\mathbf{x}$:

$$\phi_{\mathrm{ind}}\left(\mathbf{x}\right) = \frac{1}{4\pi}\left[\int_{S_b} \mu \frac{\partial}{\partial n}\frac{1}{r} - \sigma\frac{1}{r}\mathrm{d}S_b + \int_{S_{\mathrm{w}}} \mu_{\mathrm{w}}\frac{\partial}{\partial n}\frac{1}{r}\mathrm{d}S_{\mathrm{w}}\right] \tag{16}$$

Here the source strength σ on the body panels is provided by directly applying the Neumann boundary condition following Eq. (11). The spatial discretization of the bounding surfaces leads to a linear equation system which can be solved after considering the Kutta condition to calculate the doublet strengths μ. Here, the condition following Eq. (13) is replaced by using the Morino's Kutta condition $\mu_w = \mu_u - \mu_l$, to obtain the doublet strength μ_w in the wake directly behind the trailing edge, where μ_u, μ_l respectively denote the doublet strength at the upper and lower side of the trailing edge. The solution provides the unknown doublet strengths on the body panels.

*pan*MARE is coupled to *comana* and the necessary modifications for coupled simulations described in the previous section are made. The hydrodynamic forces on the structure are computed by integrating the pressure, which follows from Bernoulli's Eq. (7), over the surface. The error in the force related to the missing viscosity and friction within the potential solution is corrected by a friction model which estimates the friction force using friction coefficients c_f based on the *Schoenherr line* according to [15]. The corrected forces evaluated at the collocation points combined with the area of the panels can be used to compute the tractions necessary for the implicit coupling in Eq. (2). Since *pan*MARE is based on the potential theory, flow separation effects cannot be accounted for.

The BEM offers the benefit that only the surface of the propeller and the wake panels have to be discretized with a mesh. Therefore the complexity of the simulation is reduced by one dimension, thus making repeated simulations efficient also for optimization purposes. Furthermore, the BEM avoids having to define the outer boundaries of the fluid domain – which prevents problems with wall effects and increasing computational costs for a sufficiently large domain.

4. Structural simulation

On the structural side, the FEM implemented with the commercial solver ANSYS [10] is used within the FSI simulations.

The basis for the calculation of the deformation and motion with the FEM is the balance of linear momentum [16] defined in the reference configuration Ω:

$$\rho_0 \ddot{\mathbf{d}} = \mathrm{DIV}(\mathbf{FS}) + \rho_0 \mathbf{b}. \tag{17}$$

In Eq. (17), ρ_o is the density in the reference configuration, $\ddot{\mathbf{d}}$ is the acceleration and $\mathbf{b}$ are possible volume loads like a gravitational load. Here, $\mathbf{F}$ denotes the deformation gradient and $\mathbf{S}$ is the second Piola-Kirchhoff stress tensor.

The weak form can be derived by multiplying Eq. (17) with a test function $\boldsymbol{\eta}$, integrating over the whole domain Ω and applying integration by parts and the divergence theorem [16, p. 84]

$$\int_\Omega \rho_0 \ddot{\mathbf{d}} \cdot \boldsymbol{\eta}\,\mathrm{d}\Omega + \int_\Omega \mathbf{S}\cdot\delta\mathbf{E}\,\mathrm{d}\Omega - \int_\Omega \rho_0 \mathbf{b}\cdot\boldsymbol{\eta}\,\mathrm{d}\Omega - \int_{\Gamma_N} \mathbf{t}\cdot\boldsymbol{\eta}\,\mathrm{d}\Gamma = 0. \tag{18}$$

The traction vector $\mathbf{t}$ is integrated over the boundary Γ_N of the body defined in the reference configuration. The variation of the Green-Lagrange strain tensor is denoted as $\delta\mathbf{E}$.

After spatial discretization of the weak form Eq. (18) with the FEM and introduction of a damping matrix $\mathbf{C}$, the non-linear semi-discrete equation of motion reads

$$\mathbf{M}\ddot{\mathbf{d}} + \mathbf{C}\dot{\mathbf{d}} + \mathbf{s}(\mathbf{d}) = \mathbf{f}. \tag{19}$$

In Eq. (19), $\mathbf{M}$ is the mass matrix and $\mathbf{s}(\mathbf{d})$ is the vector of internal loads that depends non-linearly on the displacements $\mathbf{d}$. The external loads $\mathbf{f}$ stem from the integration of the fluid tractions and the volumetric load $\mathbf{b}$. The damping matrix is introduced with a stiffness proportional Rayleigh damping [17, p. 797] with a factor of $\beta = 10^{-4}$. Rayleigh damping is used to reduce oscillations that can appear in the partitioned coupled FSI simulations.

The Newmark method [18] with the parameters $\delta = \frac{1}{2}$ and $\alpha = \frac{1}{4}$ serves to solve Eq. (19). To this end, Eq. (19) is solved in an implicit way by evaluating the unknown acceleration $\ddot{\mathbf{d}}_{t+\Delta t}$, velocity $\dot{\mathbf{d}}_{t+\Delta t}$, internal load $\mathbf{s}(\mathbf{d}_{t+\Delta t})$ and external load $\mathbf{f}_{t+\Delta t}$ for the next time step $t + \Delta t$. The non-linear equation system arising from this is solved in an iterative way applying the Newton-Raphson method [16, p. 152].

In ANSYS it is possible to use different element types such as hexahedral and tetrahedral elements with first and second-order shape functions [19]. ANSYS is coupled to *comana* in order to apply tractions computed by the fluid solver to the structural mesh according to Eq. (3). Furthermore, the restart of a time step in ANSYS controlled by *comana* is realised to enable the partitioned solution procedure depicted in Figure 1.

A linear elastic material model combined with a geometrical nonlinear approach allows to capture large rotations of the structure. The $\bar{B}$-method is used in ANSYS as the standard method to prevent locking [20].

5. Ship propeller

The first example considered here is the KRISO container ship (KCS) propeller KP505. The propeller has five blades and its full-scale diameter is $D = 7.9\,\mathrm{m}$. First, the open water characteristics of the KCS propeller are computed to validate the hydrodynamic flow calculation. Since experimental data on flexible ship propellers is scarce, the validation of the thrust and torque coefficient for the ship propeller is carried out only for a rigid propeller. In this case, only one blade is considered, taking advantage of the rotational symmetry. Although the hydrodynamic problem of the propeller flow in open water can simply be treated as a stationary problem, it is considered as unsteady. This is because the hydrodynamic method should be validated with regard to the instationary FSI simulation. Therefore, it is considered as an initial boundary value problem using a fourth-order Runge-Kutta method for the time integration of the fluid simulation.

5.1. Validation of the fluid simulation

The mesh of the blade on the suction and pressure side is shown in Figure 2. Here, $18 \times 25 = 450$ panels are used on each side. The mesh is refined at the leading edge to cover the high-pressure gradients and at the blade tip to support a better roll-up of the wake.

The hydrodynamic forces, which are computed by integrating the pressure p from Bernoulli's Eq. (7) over the propeller surface, need a correction because friction is not considered in the potential theory. Taking this into account in the post-processing of each simulation step, the forces on each panel are corrected using a friction model. Applying Froude similarity, the simulation of the open water characteristics is conducted in model scale with a Froude scale ratio of $\lambda_{\mathrm{geo}} = 2.639 \cdot 10^{-2}$ in accordance with the experiments on which the validation is based. With Froude similarity, the number of revolutions per second of the propeller can be computed as $n = 9.233\,\mathrm{s}^{-1}$ based on the number of revolutions per second of the full-scale propeller, which is equal to $n = 1.5\,\mathrm{s}^{-1}$. The inflow speed v_∞ is changed so that the advance ratio

$$J = \frac{v_\infty}{n\,D}\,, \tag{20}$$

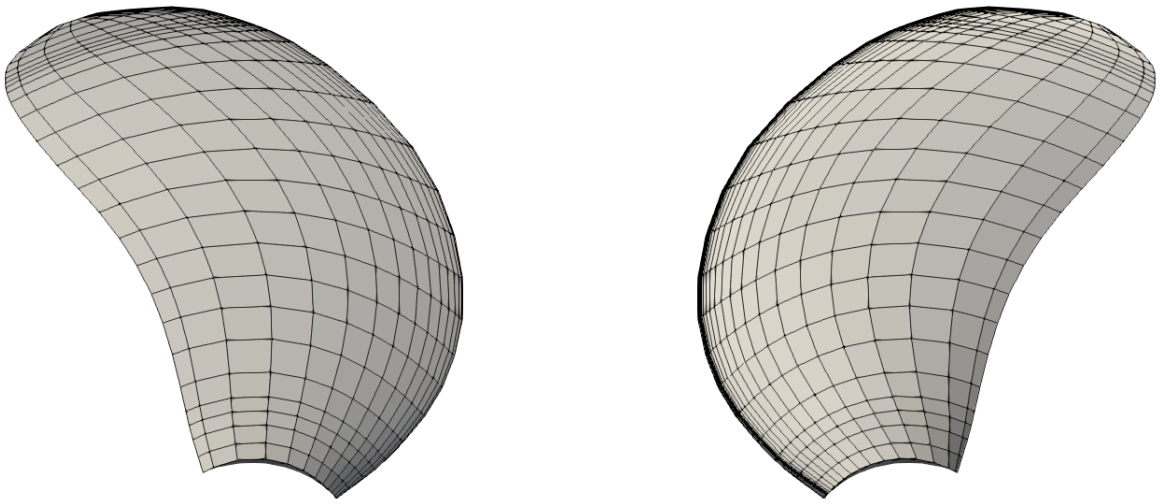

(a) Suction side (b) Pressure side

Figure 2: Mesh of the KCS propeller blade.

Table 1: Parameters for the model scale rigid body ship propeller simulation.

quantity	value
Froude scale ratio λ_{geo}	$2.639 \cdot 10^{-2}$
blade count z	5
revolutions per second n	$9.233\,\frac{1}{\text{s}}$
angle increment $\Delta\alpha_t$	2°
diameter D	$0.208\,\text{m}$
advance ratio J	$0.5 - 0.9$
time step size Δt	$6.02 \cdot 10^{-4}\text{s}$

varies in the range $J \in [0.5, 0.9]$. The resulting parameters are listed in Table 1. The time step is selected in such a way that the propeller turns 2° in every time step.

160 Each simulation is conducted until the hydrodynamic force $\mathbf{F}_h = (F_{h,x}, F_{h,y}, F_{h,z})^T$ and the associated moment $\mathbf{M}_h$ on the propeller blade are converged. Then the thrust $T = z(\mathbf{n}_\alpha \cdot \mathbf{F}_h)$ and the torque $Q = z(\mathbf{n}_\alpha \cdot \mathbf{M}_h)$, with $\mathbf{n}_\alpha$ being the normalized vector pointing in the axis of propeller rotation and z being the number of blades of the propeller, are determined.

In Fig. 3 the open water characteristics of the KCS propeller computed by *pan*MARE are plotted and compared with experimental (EFD) data published in [21]. Here, the solid lines denote the thrust coefficient k_T, the dashed lines denote the torque coefficient k_Q and the dash-dotted lines denote the efficiency η_0. The

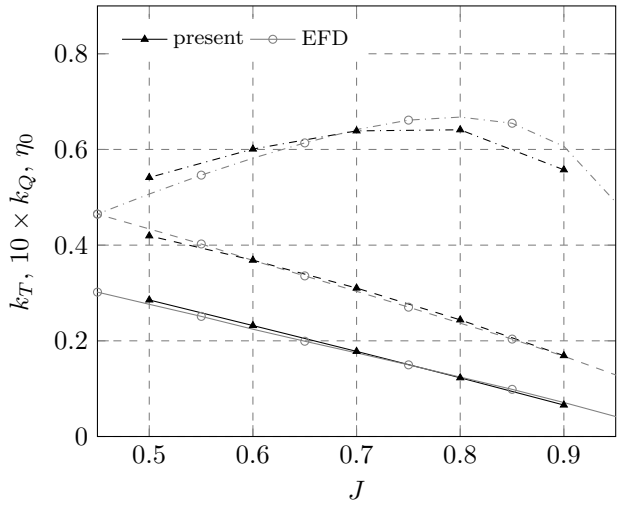

Figure 3: Open water diagram of KCS computed by *pan*MARE (present) and compared with experimental data (EFD) [21].

characteristic values are plotted against the advance ratio J, and they are defined as follows:

$$k_T = \frac{T}{\rho\, n^2\, D^4}\,, \tag{21}$$

$$k_Q = \frac{Q}{\rho\, n^2\, D^5}\,, \tag{22}$$

$$\eta_0 = \frac{J}{2\pi}\frac{k_T}{k_Q}\,. \tag{23}$$

Fig. 3 shows a good agreement between the experimental data and the simulations conducted with *pan*MARE. For the thrust and torque coefficients, only a slight deviation is visible in the region of low advance ratios. Closer to the operating conditions in the range of $J = 0.7 - 0.8$ the rigid body fluid simulations agree very well with the experimental data.

5.2. FSI simulation of the KCS propeller

In the coupled simulation, the start-up of the simulation is more challenging than in a rigid body fluid simulation. Since a direct start of the simulation at full rotational speed is currently not possible on the structural side, the rotational speed of the propeller must be increased slowly. The rotational motion of the propeller blade is realized by prescribing displacements on the hub of the propeller blade. Displacements on the hub corresponding to a certain rotation angle α can be prescribed from *comana*. To initialize the simulation, the rotational angle is incremented with a ramp until full rotational speed is obtained. The rotational angle α at time t is computed as $\alpha_t = \alpha_{t-\Delta t} + \Delta\alpha_t$. The angle increment is computed with a cosine

$$\Delta\alpha_t = 0.5\,\alpha_{full}\left(1 - \cos\left(\frac{t}{t_{rot,e}}\pi\right)\right). \tag{24}$$

If t is larger than $t_{rot,e}$ the angle increment $\Delta\alpha_t$ is set to the full increment of $\Delta\alpha_{full} = 2°$. The resulting angle increment over the time step is shown in Figure 4 for $t_{rot,e} = 180\Delta t$. The time step size is the same in the structural and fluid solver, chosen such that, after the full rotational speed is obtained, the angle increment is equal to 2° in one time step.

When the displacements of the structural solver are transferred to the fluid solver according to Eq. (2), a displacement correction technique as described in [22] is used. After full rotational speed is reached, the

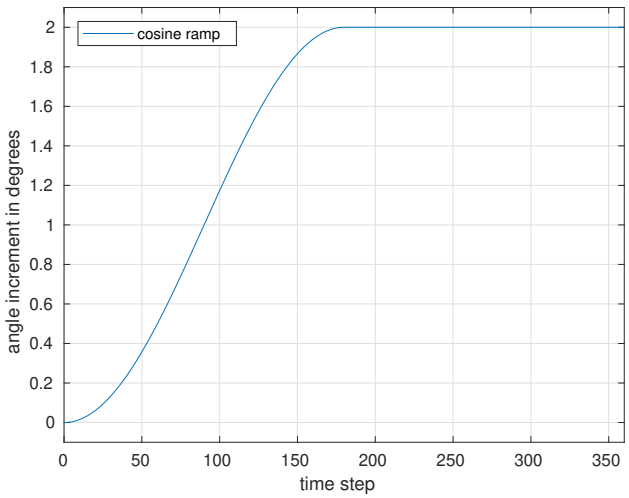

Figure 4: Ramp to accelerate the propeller to full rotational speed.

tractions that are computed by the fluid solver are also applied with a ramp in order to avoid instabilities due to abrupt application of loads. The factor

$$\beta_{tr} = 0.5 \left(1 - \cos\left(\frac{t - t_{tr,st}}{t_{tr,e}}\pi\right)\right) \tag{25}$$

is included in Eq. (3) such that $\mathbf{d}_i^t = \mathcal{S}(\beta_{tr}\mathbf{t}_i^t)$. If the time t is lower than $t_{tr,st}$, β_{tr} is set to zero. If it is bigger than $t_{tr,e}$, β_{tr} is set to one.

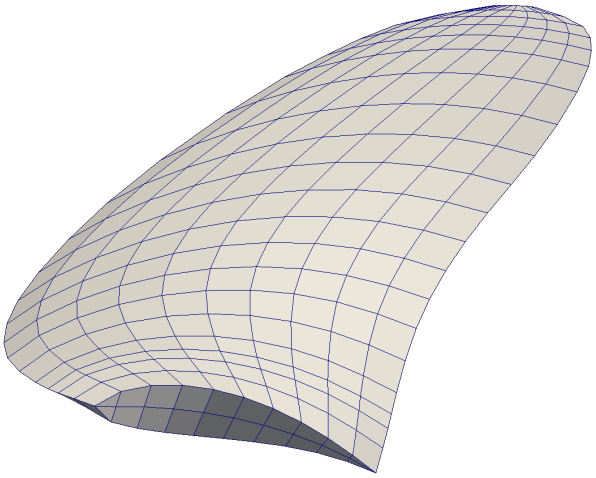

Figure 5: Layered structural mesh with hub surface and suction side.

Tractions computed by *pan*MARE are applied to ANSYS on the pressure and suction side of the propeller through *comana*.

The meshing of a propeller blade is challenging due to the high curvature of the surface. As mentioned in Section 1, the simulations and meshes developed here should be used to optimize the propeller shape. To this end, it is important to mesh the propeller with a generic approach that can also be adapted to strongly

Table 2: Parameters for the FSI ship propeller simulation.

quantity	value
Froude scale ratio λ_{geo}	1
blade count z	5
revolutions per second n	$1.5\,\frac{1}{\text{s}}$
angle increment $\Delta\alpha_t$	2°
diameter D	$7.9\,\text{m}$
advance ratio J	$0.4 - 1.0$
time step size Δt	$\frac{1}{270}\,\text{s}$
total simulation time t_e	$1800\Delta t$
time of full rotational speed $t_{rot,e}$	$180\Delta t$
traction ramp start $t_{tr,st}$	$540\Delta t$
traction ramp end $t_{tr,e}$	$590\Delta t$

modified geometries. In addition, a structured layered meshing approach is used since it can give better results for different propeller geometries compared to e.g. automatic meshing approaches.

The whole geometry of the propeller is described by B-spline surfaces [23, p. 486], which contain the hub surface, the tip surface, the pressure side and the suction side of the propeller. A structured surface mesh is constructed by evaluating the B-spline surfaces of both sides on the propeller blade at a regular distance in both of the local coordinates of the B-spline surface. A layered volume mesh is then generated by linearly interpolating the corresponding coordinates on both sides of the propeller. To reduce the number of elements with a high aspect ratio and angles close to 0° or 180°, the tip of the propeller blade is cut-off. The elements that are used for the ship propeller are linear hexahedral elements. The resulting mesh is depicted in Figure 5. Due to the fact that the surface of the suction and the pressure side of the propeller blade run together at the leading and trailing edge of the propeller blade, wedge elements are used along these edges. These wedge elements are generated in ANSYS as degenerated hexahedral elements.

The translational velocity v_∞ of the ship propeller is varied according to Eq. (20) depending on the chosen advance ratio. The most important parameters for the simulation are summarised in Table 2.

To investigate the influence of a flexible propeller blade compared to a rigid propeller blade, the Young's modulus is varied between $5 \cdot 10^9\,\text{Pa}$ (close to the Young's modulus of polymers) and $2 \cdot 10^{11}\,\text{Pa}$ (close to the Young's modulus of steel). The Poisson ratio ν is set to 0.3 and the density to $7750\,\frac{\text{kg}}{\text{m}^3}$.

The results of the KCS propeller in open water conditions for the thrust coefficient k_T, the torque coefficient k_Q, and the efficiency η_0 are depicted in Fig. 6. A comparison between the results for the rigid body simulation in *pan*MARE and the coupled simulation with *comana* with a Young's modulus of $2 \cdot 10^{11}\,\frac{\text{N}}{\text{m}^2}$ shows that the influence of the deflection on the parameters of a propeller is negligible for a high stiffness (like a steel propeller). The difference between these two cases is below 0.5 % for k_T and k_Q and therefore the assumption of a rigid propeller for a material with high stiffness is valid for these propellers. The difference to a rigid propeller remains small – even for a Youngs modulus down to $5 \cdot 10^{10}\,\frac{\text{N}}{\text{m}^2}$, which is below the Youngs modulus of most metal alloys used in practice.

For low advance ratios, the torque and thrust are increased initially with decreasing stiffness for this propeller. The increase of the necessary torque is larger compared to the increase in thrust, leading to a lower overall efficiency according to Eq. (23). For a Young's modulus of $5 \cdot 10^9\,\frac{\text{N}}{\text{m}^2}$ and an advance ratio of $J = 0.4$ the thrust is lower compared to that of a rigid propeller – while the necessary torque is increased, leading to significantly lower efficiency. For an advance ratio of $J = 0.8$, which is closer to operating conditions, the thrust and torque coefficients remain almost unaffected for the considered range of Young's moduli. For high advance ratios above $J = 0.8$, the torque and thrust are reduced for propellers with lower stiffness – which, in combination, once again leads to a lower efficiency. If the advance ratio is equal to 1, thrust

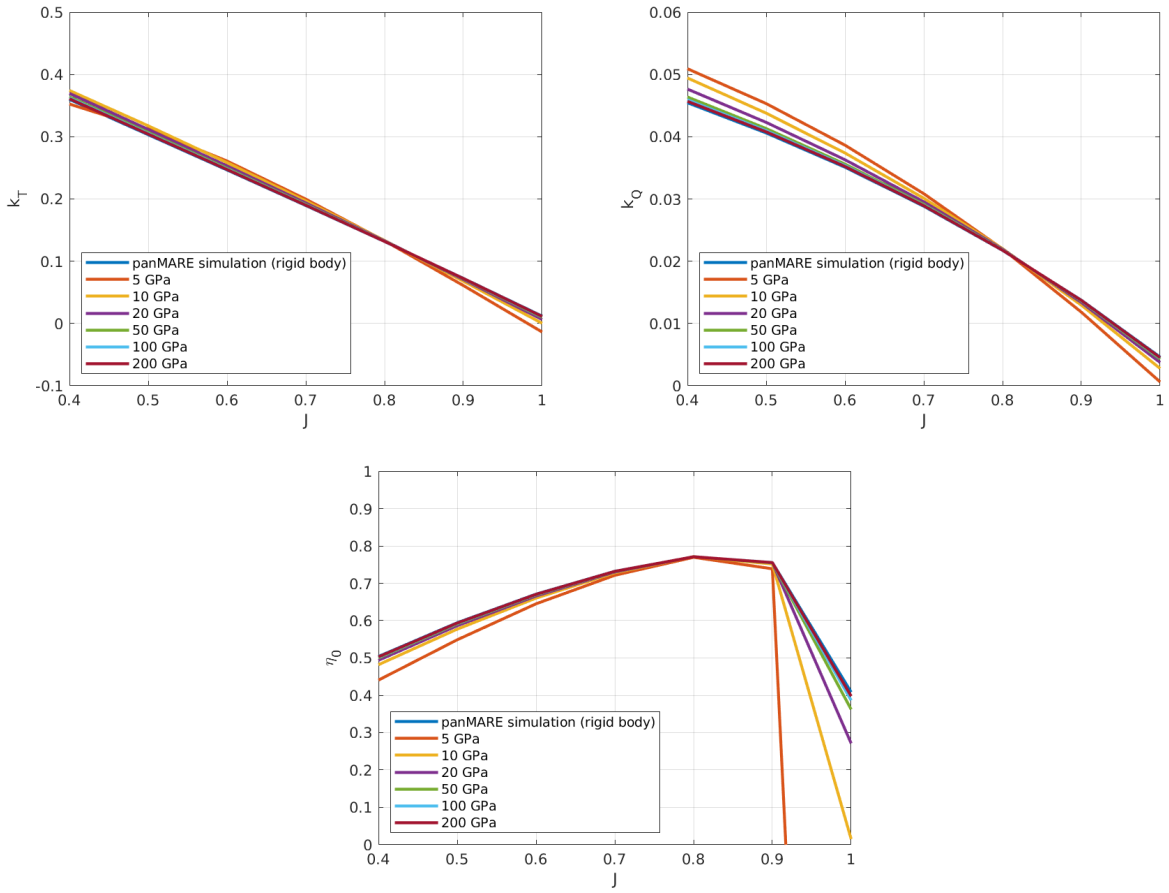

Figure 6: k_T, k_Q, and η_0 for varying advance ratios and Young's modulus.

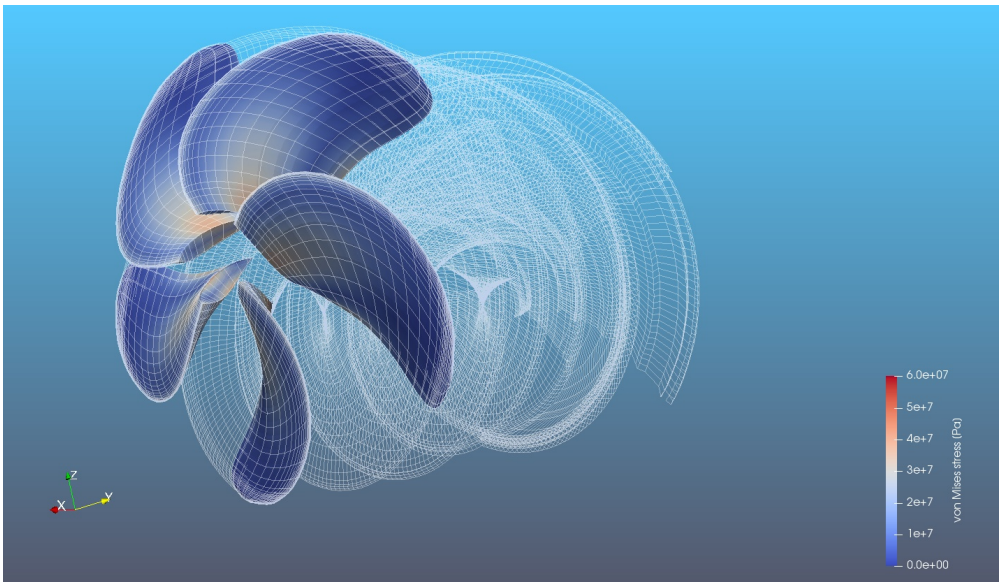

Figure 7: Equivalent stress of full KCS propeller with wake.

becomes negative for very flexible propellers.

Even though the influence of the deformation of the structure on the fluid field is negligible for a propeller with a high stiffness, the approach presented here also offers distinct advantages for these propellers. The coupling enables an instantaneous evaluation of the stresses inside the propeller at every location. It is also possible to evaluate more complex loading conditions such as the loading of a propeller in the ship wake during full rotation. Fig. 7 shows the von Mises equivalent stress for a ship propeller for an inflow field that resembles a ship wake.

In order to validate the full FSI-approach another example is considered in the next section.

6. Multilayered submersible mixer

The next example considered here is a multilayered submersible mixer taken from the experimental work of Lass [24], carried out at the University of Rostock. A submersible mixer is used as a mixing device, e.g. in the chemical industry or in sewage plants, and it generates a complex flow field in order to mix the fluids thoroughly.

The mixer was tested in a closed-loop channel so that it generated its own inflow field by creating a circular flow in the channel [24, p.64]. The inflow velocity on the propeller in the main flow direction was measured, as well as the torque and the thrust acting on the mixer. Using strain gauges [24, p.67] the strains inside the propeller were measured at specific locations, allowing a comparison with the strains computed by the FSI simulation approach presented in this work.

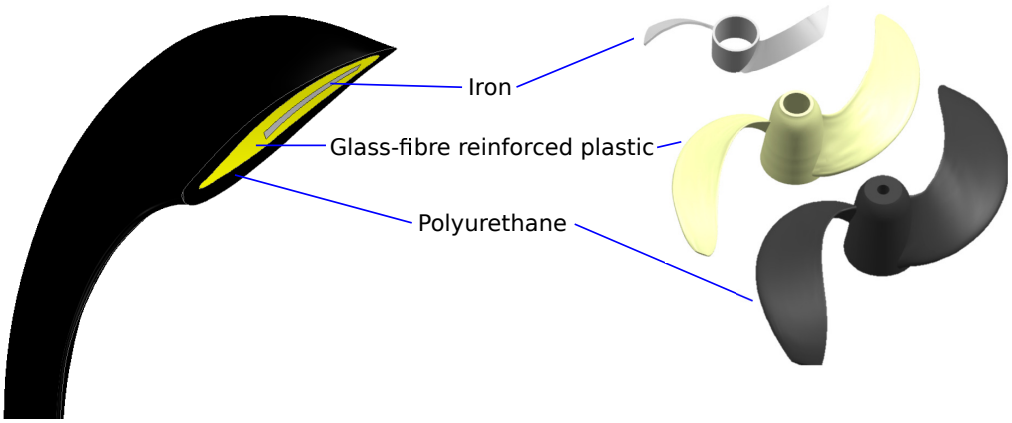

Figure 8: Structure of the multilayered submersible mixer [24, p.62].

In contrast to the ship propeller presented in the previous section, the multilayered mixer does not have constant material properties but consists of three different layers, as shown in Fig. 8. The inner ring of the mixer consists of an iron stiffener, which is encapsulated by a glass-fibre reinforced plastic (GFRP) layer. The strain gauges are applied on the GFRP layer, and a polyurethane resin layer is moulded on the GFRP layer to protect the strain gauges and the cable system from short circuits. The constitutive behaviour is modelled with an isotropic linear elastic material model applying the parameters given in Table 4.

Due to the multilayered material of the mixer, the approach presented in Section 4 for the purpose of generating the mesh cannot be applied for this structure. Therefore, automatically generated second-order tetrahedral meshes are obtained using ANSYS. The algorithm used in ANSYS to generate the mesh is based on Voronoi Delaunay triangulation [25]. Since the strain is very sensitive to the mesh resolution in the structural simulation, the coupled FSI simulation is conducted with three different mesh densities. The

Table 3: Parameters for the submersible mixer simulation.

quantity	value
Froude scale ratio λ_{geo}	1
blade count z	2
revolutions per second n	$4.0\bar{3}\,\frac{1}{\text{s}}$
angle increment $\Delta\alpha_t$	2°
radius r	$0.455\,\text{m}$
axial inflow velocity v_a	$0.28\,\frac{\text{m}}{\text{s}}$
advance ratio J	0.08
time step size Δt	$0.0001377\,\text{s}$
total simulation time t_e	$1800\Delta t$
time of full rotational speed $t_{rot,e}$	$180\Delta t$
traction ramp start $t_{tr,st}$	$360\Delta t$
traction ramp end $t_{tr,e}$	$410\Delta t$

Table 4: Material properties of the submersible mixer [24, p. 87].

material	Young's modulus	Poisson number	density
iron	$1.1 \cdot 10^{11}\,\frac{\text{N}}{\text{m}^2}$	0.28	$7200\,\frac{\text{kg}}{\text{m}^3}$
GFRP	$3.3 \cdot 10^{9}\,\frac{\text{N}}{\text{m}^2}$	0.27	$1500\,\frac{\text{kg}}{\text{m}^3}$
polyurethane	$1.4 \cdot 10^{9}\,\frac{\text{N}}{\text{m}^2}$	0.35	$1200\,\frac{\text{kg}}{\text{m}^3}$

coarse structural mesh contains 41,943 degrees of freedom (DOF), the medium mesh 82,581 DOF and the fine mesh 206,337 DOF. The coarse structural mesh is depicted in Figure 10.

Figure 9 shows the grid of the suction and pressure side of one blade of the submersible mixer used for the hydrodynamic simulation. The grid is refined at the leading edge to cover the high-pressure gradients in this range. The total number of panels for each blade is $35 \times 80 = 2800$. The advance ratio J of the submersible mixer follows from Eq. (20) using the averaged axial inflow velocity [24, p.62].

The inflow velocity on the mixer is unsteady in the experiment, the standard deviation of the inflow velocity in some regions is high compared to the mean inflow velocity on the mixer [24, p.74]. The inflow on the propeller is only measured in the main flow direction (x-direction), but not in the y- and z-direction, even though the complex flow field indicates significant flow components in these directions, due to vortices and submerged flows [24, p.75].

Fig. 11 shows results for the thrust and torque coefficient (averaged over time) for the rigid body simulation with *pan*MARE and for the fully coupled FSI simulation. The results of the uncoupled (rigid body) simulation with *pan*MARE are compared with fluid simulations conducted by Lass [24] who uses an unsteady vortex lattice method (UVLM). Both methods have in common that they are based on potential theory. However, in contrast to the present boundary element method, UVLM assumes that the lifting surfaces are thin, neglecting the thickness of the blade. The comparison for the uncoupled simulation approach shows a good agreement with the UVLM approach.

For the validation of the coupled solution approach, simulations with *comana* as described above are compared to the experimental results obtained with the flexible submersible mixer. The mean value is computed over two full rotations with a filter to exclude outliers due to numerical uncertainties. The numerical uncertainties stem from small distorted panels at the tip of the propeller. Due to the deformation of the mixer, the distortion of these small panels is aggravated. The comparison of the fully coupled FSI

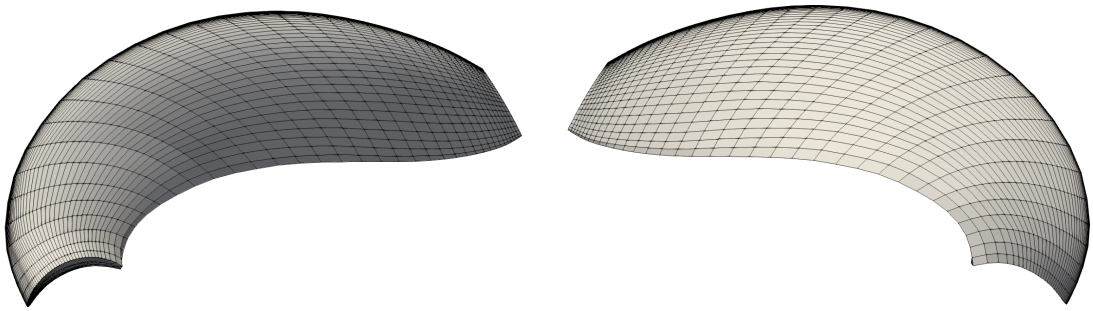

(a) Suction side. (b) Pressure side.

Figure 9: Mesh of submersible mixer for hydrodynamic simulation.

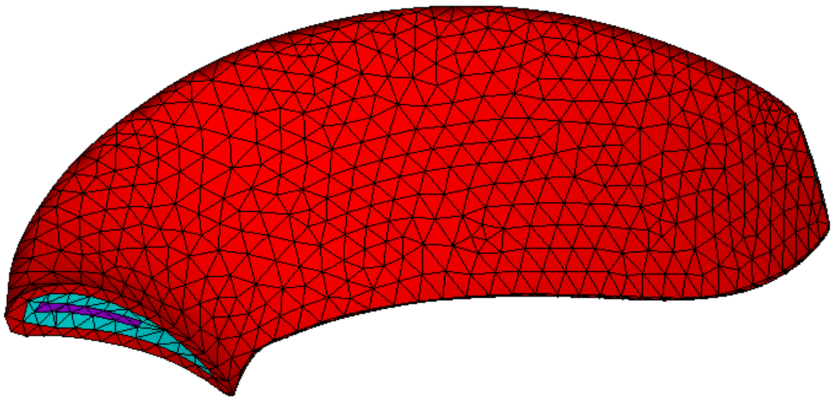

Figure 10: Coarse mesh of the submersible mixer for structural simulation – with different colours for the different layers.

simulations with the experiment is shown in Fig. 11. The captured k_T coefficient of the FSI simulations agrees very well with the thrust measured in the experiment even though only the axial velocity component is considered in the simulation. For the torque, a significant deviation of approximately 10% between the k_Q value of the experiment and the k_Q value computed in the FSI simulation is visible. The experimental data for the torque show a high systematic measurement uncertainty, indicated in Fig. 11 [24, p.65]. This uncertainty might explain the difference between the fully coupled FSI simulation and the experimental results for the torque coefficient. Also, the presence of vortices that are not captured in the constant axial inflow velocity could be an explanation for the higher torque in the experiment compared to the FSI simulation.

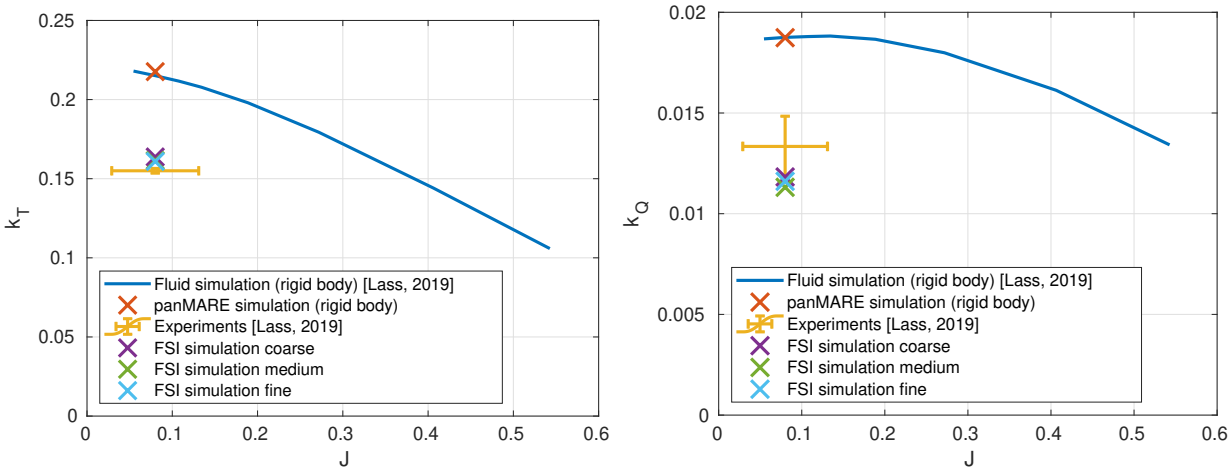

Figure 11: Thrust and torque coefficients for experiment and simulations.

To further validate the coupled solution approach, the strains in the experiment measured with strain gauges are also compared to the strains computed with the coupled approach in ANSYS. The strains are compared based on the von Mises equivalent strain, which is defined based on the three principal strains ε_1, ε_2 and ε_3 analogously to the von Mises equivalent stress according to Eq. (26) [26, p. 831] [27, p. 203]

$$\varepsilon_{vM} = \frac{1}{1+\nu}\sqrt{\frac{1}{2}\left[(\varepsilon_1-\varepsilon_2)^2+(\varepsilon_2-\varepsilon_3)^2+(\varepsilon_3-\varepsilon_1)^2\right]}. \tag{26}$$

For the experimental measurement, the strain gauges are glued onto the surface of the GFRP layer before the polyurethane layer is moulded on top. The definition of the von Mises equivalent strain Eq. (26) is chosen such that it is in accordance with the definition used in the experiment [24, p.68].

The strains measured in the experiment [24, p.77] for the strain gauges labelled 4-6 in Fig. 12b are compared to the strains computed with the coupled FSI simulation. In the FSI simulation, the von Mises strain according to Eq. (26) is used.

The results for the comparison are shown in Fig. 12a. The location of the strain gauges can be seen in Fig. 12b, while Fig. 12c shows the strain distribution of the von Mises strain on the surface of the GFRP layer computed with the FSI simulation.

A good agreement between the experimental measurements and the strains computed in the FSI simulation is visible for strain gauges 4 and 6. For strain gauge number 5, a significant deviation between the experiment and the simulation is visible. A possible explanation for this difference is an uncertainty in the exact location of the strain gauge in the experimental measurement. The strain distribution shows a maximum in the spanwise region where the iron stiffener ends close to the leading edge of the blade.

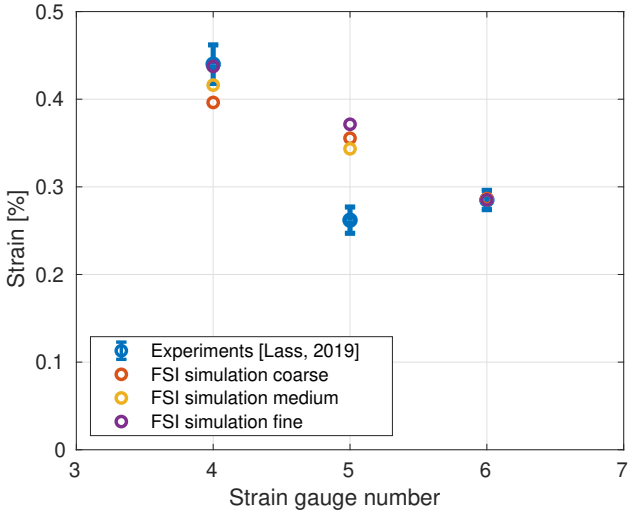

(a) Comparison of the experiment with the FSI simulation.

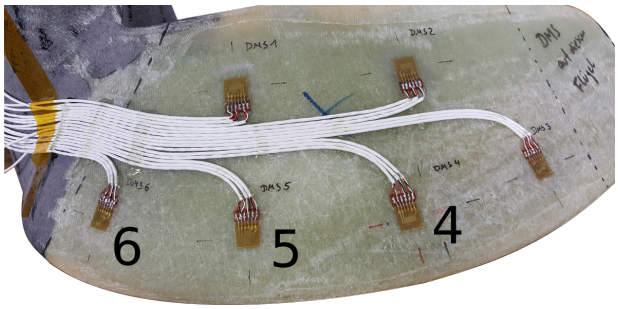

(b) Location of strain gauges [24, p.67].

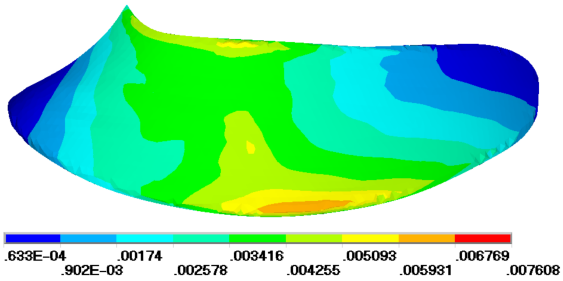

(c) Strain distribution on the GFRP layer.

Figure 12: Validation based on the strain.

7. Conclusion and outlook

A partitioned approach for the FSI simulation of flexible propellers and the rotor of mixers was presented – including a description of the solving of the fluid subproblem with the in-house developed BEM solver *pan*MARE and the solving of the structural problem with the commercial FEM solver ANSYS. Two quite different examples of turbo machine rotors are considered. The first example is a typical ship propeller geometry (KCS propeller), as used for the propulsion of commercial vessels, and the second example is the rotor of a submersible mixer that is used for mixing in industrial applications.

For the ship propeller, the thrust and torque coefficient for different advance ratios and Young's modulus are presented. Since no experimental data is available for the thrust and torque coefficient of flexible ship propellers, the validation of the ship propeller example is only conducted for the rigid body fluid simulation in *pan*MARE. In conclusion, the results of the simulations agree well with the experimental results. For a stiff ship propeller, the rigid body simulation in *pan*MARE shows a good agreement with the available experimental data.

The benefit of the fully coupled FSI simulation lies in the possibility to capture the thrust and torque as well as other parameters more accurately compared to rigid body fluid simulations. Furthermore, the FSI simulation allows to evaluate the structural fields, e.g. the stress and strain fields, in every loading state in the operational condition of a ship propeller.

To validate the FSI simulation, the thrust and torque coefficients as well as the strains of the submersible mixer presented in Section 6 are compared with the experiments conducted in [24] and the FSI simulations with *comana*, ANSYS and *pan*MARE. The comparison shows a good agreement for the thrust coefficient. The deviation between the measured and calculated torque coefficient is in the range of the uncertainty of the torque measurement. Another possible reason for differences in the torque and thrust between the experiment and the simulation is the existence of vortices which lead to flow components perpendicular to the main flow direction, which cannot be captured in the FSI simulations. The comparison for the strain also shows a very good agreement for two of the three strain gauges.

In conclusion, the validation shows that the FSI approach presented in this paper is able to accurately capture the deformation of the submersible mixer and the effect on the flow field measured with the torque

and thrust coefficient.

In future works, the framework developed and shown here should be used to optimise the shape and material of a ship propeller, based on coupled FSI simulations, in order to reduce cavitation and noise emissions while maintaining thrust and improving efficiency.

Acknowledgements

The authors gratefully acknowledge the support provided by the DFG (German Science Foundation Deutsche Forschungsgemeinschaft) under the grant number DU 405/13-2, AB 112/12-2 and the project number 344826971.

The authors are very grateful to Prof. Dr.-Ing. Frank-Hendrik Wurm and Dr.-Ing. Andre Lass, Univeristy of Rostock, for providing the valdidation data and their support in the interpretation of the experimental and numerical results.

Disclosure statement

No potential conflict of interest was reported by the authors.

References

[1] Class NK, Nakashima Propeller, ClassNK and Nakashima Propeller Announce Worlds First Installation of a CFRP Propeller on a Merchant Vessel, https://www.classnk.or.jp/hp/en/hp_news.aspx?id=1043&type=press_release&layout=1, press release (August 2014).

[2] T. Lampe, L. Radtke, M. Abdel-Maksoud, A. Düster, A partitioned solution approach for the simulation of dynamic behaviour and acoustic signature of flexible cavitating marine propellers, Ocean Engineering 197 (2020) 106854. doi:10.1016/j.oceaneng.2019.106854.

[3] L. Radtke, T. Lampe, M. Abdel-Maksoud, A. Düster, Partitioned simulation of the acoustic behavior of flexible marine propellers using finite and boundary elements, PAMM 20 (1) (2021) e202000315. doi:10.1002/pamm.202000315.

[4] Z. Liu, Y. L. Young, Utilization of deformation coupling in self-twisting composite propellers, in: Proceedings of 16th International Conference on Composite Materials, Kyoto, Japan, 2007, pp. 8–13.

[5] Y. L. Young, Hydroelastic behavior of flexible composite propellers in wake inflow, in: Proceedings of 16th International Conference on Composite Materials, Kyoto, Japan, 2007, pp. 1–6.

[6] Y. Bazilevs, K. Takizawa, T. E. Tezduyar, Computational fluid-structure interaction: methods and applications, John Wiley & Sons, Ltd, 2013. doi:10.1002/9781118483565.

[7] H. Bungartz, M. Schäfer (Eds.), Fluid-Structure Interaction, Modelling, Simulation and Optimisation, Vol. 53 of Lecture Notes in Computational Science and Engineering, Springer, 2006. doi:10.1007/3-540-34596-5.

[8] H. Bungartz, M. Mehl, M. Schäfer (Eds.), Fluid-Structure Interaction II, Modelling, Simulation, Optimisation, Vol. 73 of Lecture Notes in Computational Science and Engineering, Springer, 2010. doi:10.1007/978-3-642-14206-2.

[9] M. Bauer, M. Abdel-Maksoud, A 3-d potential based boundary element method for modelling and simulation of marine propeller flows, IFAC Proceedings Volumes 45 (2) (2012) 1179–1184. doi:10.3182/20120215-3-AT-3016.00209.

[10] ANSYS, Ansys academic research mechanical, release 19.2 (2018).

[11] M. König, L. Radtke, A. Düster, A flexible C++ framework for the partitioned solution of strongly coupled multifield problems, Computers & Mathematics with Applications 72 (7) (2016) 1764–1789. doi:10.1016/j.camwa.2016.07.031.

[12] J. Degroote, K.-J. Bathe, J. Vierendeels, Performance of a new partitioned procedure versus a monolithic procedure in fluid-structure interaction, Computers and Structures 87 (2009) 793–801. doi:10.1016/j.compstruc.2008.11.013.

[13] L. Radtke, A. Larena-Avellaneda, E. S. Debus, A. Düster, Convergence acceleration for partitioned simulations of the fluid-structure interaction in arteries, Computational Mechanics 57 (6) (2016) 901–920. doi:10.1007/s00466-016-1268-0.

[14] J. Katz, A. Plotkin, Low speed aerodynamics, second edition Edition, Cambridge aerospace series, Cambridge University Press, Cambridge, 2001. doi:10.1017/CBO9780511810329.

[15] S. F. Hoerner, Fluid-Dynamic Drag - Practical Information on Aerodynamic Drag and Hydrodynamic Resistance, Hoerner Fluid Dynamics, 1965. doi:10.1017/S0001924000034187.

[16] P. Wriggers, Nonlinear Finite Element Methods, Springer Berlin Heidelberg, Berlin, Heidelberg, 2008. doi:10.1007/978-3-540-71001-1.

[17] K.-J. Bathe, Finite element procedures, Klaus-Jurgen Bathe, 2014. doi:10.1002/9780470050118.ecse159.

[18] N. M. Newmark, A method of computation for structural dynamics, Journal of the engineering mechanics division 85 (3) (1959) 67–94. doi:10.1061/JMCEA3.0000098.

[19] ANSYS, Mechanical APDL Element Reference, Release 19.2, ANSYS, Inc., Southpointe (2018).

[20] T. J. Hughes, Generalization of selective integration procedures to anisotropic and nonlinear media, International Journal for Numerical Methods in Engineering 15 (9) (1980) 1413–1418. doi:10.1002/nme.1620150914.

[21] J. Otzen, P. Esquivel, C. Simonsen, F. Stern, CFD and EFD Prediction of Added Powering of KCS in Regular Head Waves, in: 32nd Symposium on Naval Hydrodynamics, 2018, pp. 5–10.

[22] L. Radtke, T. Lampe, M. Abdel-Maksoud, A. Düster, A partitioned solution approach for the simulation of the dynamic behaviour of flexible marine propellers, Ship technology research 67 (1) (2020) 37–50. doi:10.1080/09377255.2018.1542782.

[23] L. Schumaker, Spline Functions: Basic Theory, 3rd Edition, Cambridge Mathematical Library, Cambridge University Press, 2007. doi:10.1017/CBO9780511618994.

[24] A. Lass, Simulation der Rotordynamik gehäuseloser Strömungsmaschinensysteme mit flexiblen Rotorblättern im Zeitbereich - Entwicklung eines Modellierungsansatzes und experimentelle Validierung anhand eines Tauchmotorrührwerkes, Ph.D. thesis, Universität Rostock (2019). doi:10.18453/rosdok_id00002967.

[25] P.-L. George, F. Hecht, É. Saltel, Fully automatic mesh generator for 3d domains of any shape, IMPACT of Computing in Science and Engineering 2 (3) (1990) 187–218. doi:https://doi.org/10.1016/0899-8248(90)90012-Y.

[26] ANSYS, Mechanical APDL Theory Reference, Release 19.2, ANSYS, Inc., Southpointe (2018).

[27] B. Szabó, I. Babuška, Finite element analysis, John Wiley & Sons, 1991.